Numerical Modeling of Seismic and Displacement-Based Monitoring for the EGS Collab Project

Lianjie Huang[1], Yu Chen[1], Kai Gao[1], Pengcheng Fu[2], Joseph Morris[2], Jonathan Ajo-Franklin[3], Seiji Nakagawa[3], and EGS Collab Team[4]

[1]Los Alamos National Laboratory, Los Alamos, NM 87545, USA
[2]Lawrence Livermore National Laboratory, Livermore, CA 94551, USA
[3]Lawrence Berkeley National Laboratory, Berkeley, CA 94720, USA

Keywords

Active seismic, anisotropic media, elastic-wave sensitivity, enhanced geothermal systems (EGS), finite-element modeling, fracturing, monitoring, passive seismic, strain, tilt.

ABSTRACT

Reliable monitoring of fractures created during water/fluid injection in enhanced geothermal systems (EGS) is crucial for understanding the efficacy of the fracturing process. The EGS Collab project is a new research effort initiated by the US DOE Geothermal Technologies Office (GTO) to study the rock mass response to simulation. We conduct numerical modeling of active and passive seismic monitoring and alternative displacement-type measurement for monitoring hydraulic fracturing growth at the EGS Collab experiment site. We perform elastic-wave sensitivity propagation to provide the best locations to place geophones to record most significant information reflected/transmitted/scattered from the fracture plane. Our numerical results show that the optimal locations to record significant seismic signals from the fracture plane are within an anisotropic spatial region. For cost-effective passive seismic monitoring, we study the relationships between standard deviation errors of micro-earthquake locations and

---

[4]J. Ajo-Franklin, S.J. Bauer, T. Baumgartner, D. Blankenship, A. Bonneville, L. Boyd, S.T. Brown, J.A. Burghardt, S.A. Carroll, T. Chen, C. Condon, P.J. Cook, P.F. Dobson, T. Doe, C.A. Doughty, D. Elsworth, L.P. Frash, Z. Frone, P. Fu, A. Ghassemi, H. Gudmundsdottir, Y. Guglielmi, G. Guthrie, B. Haimson, J. Heise, C.G. Herrick, M. Horn, R.N. Horne, M. Hu, H. Huang, L. Huang, T.C. Johnson, B. Johnston, S. Karra, K. Kim, D.K. King, T. Kneafsey, H. Knox, D. Kumar, M. Lee, K. Li, M. Maceira, N. Makedonska, C. Marone, E. Mattson, M.W. McClure, J. McLennan, T. McLing, R.J. Mellors, E. Metcalfe, J. Miskimins, J.P. Morris, S. Nakagawa, G. Neupane, G. Newman, A. Nieto, C.M. Oldenburg, R. Pawar, P. Petrov, B. Pietzyk, R. Podgorney, Y. Polsky, S. Porse, B. Roggenthen J. Rutqvist, H. Santos-Villalobos, P. Schwering, V. Sesetty, A. Singh, M.M. Smith, N. Snyder, H. Sone, E.L. Sonnenthal, N. Spycher, C.E. Strickland, J. Su, A. Suzuki , C. Ulrich, N. Uzunlar, C.A. Valladao, W. Vandermeer, D. Vardiman, V.R.. Vermeul, J.L. Wagoner, H.F. Wang, J. Weers, J. White, M.D. White, P. Winterfeld Y.S. Wu, Y. Wu, Y. Zhang, Y.Q. Zhang, J. Zhou, Q. Zhou, M.D. Zoback

geophone distributions within multiple monitoring wells. Our results show that only two geophones per well are required for reliable event location, and that the combination of parallel and perpendicular wells does not help with MEQ event location. We conduct finite-element modeling to study the feasibility of using alternative displacement-type measurement to monitor hydraulic fracturing growth at the EGS Collab experiment site. Our numerical modeling results can help determine the geophysical monitoring strategy during the EGS Collab experiments.

1. Introduction

Hydraulic simulation is usually used in enhanced geothermal systems (EGS) to create fractures. Geophysical monitoring is a key component for the EGS Collab (Stimulation Investigations for Geothermal Modeling Analysis and Validation) project initiated and supported by the US DOE Geothermal Technologies Office (GTO). This is a Collaborative research project among multiple US Department of Energy's national labs and universities to study the rock mass response to simulation. The objective of this project is to address fundamental challenges in understanding the relationship between permeability creation, seismicity, and reservoir/heat production in crystalline rocks under relevant stress and temperature conditions, with a vision to validate and verify computational models using advanced monitoring methods that can be leveraged for the Frontier Observatory for Research in Geothermal Energy (FORGE) EGS field laboratory, the DOE flagship EGS research effort.

The EGS Collab project has chosen the Sanford Underground Research Facility (SURF) in South Dakota as the experimental site (Kneafsey, et al, 2017). Multiple boreholes will be used for geophysical monitoring of fractures creation during stimulation. It is essential to understand the optimal distributions of geophysical sensors for cost-effective monitoring.

We conduct numerical modeling of elastic-wave sensitivity propagation in an anisotropic medium built using laboratory measurements of core samples from the SURF site. The 3D spatial distribution of elastic-wave sensitivity energies can be used to guide geophone placements to acquire most significant reflected/transmitted/scattered elastic-waves from an active seismic source.

For cost-effective microseismic monitoring, we study the relationship between the standard deviation errors of event locations of micro-earthquakes and geophone distributions for various combinations of monitoring wells, either parallel with or perpendicular to the fracture plane.

In addition, we perform finite-element modeling to study the feasibility of using alternative displacement-type measurement to monitor hydraulic fracturing growth at the EGS Collab experiment site.

2. Numerical Modeling of Elastic-Wave Sensitivity in Anisotropic Media

A multi-level continuous active source seismic monitoring (ML-CASSM) (Daley, et al, 2007) will be used to acquire active seismic data at SURF for fracture imaging. The ML-CASSM systems will be installed within the monitoring wells as illustrated in Figure 1. In our following numerical modeling for seismic monitoring, we assume the distances between the boreholes parallel with the fracture zone in the blue circular region are all 5 m. We conduct numerical

modeling of elastic-wave sensitivity propagation for sources located at the dark balls “1” and “2” in Figure 1.

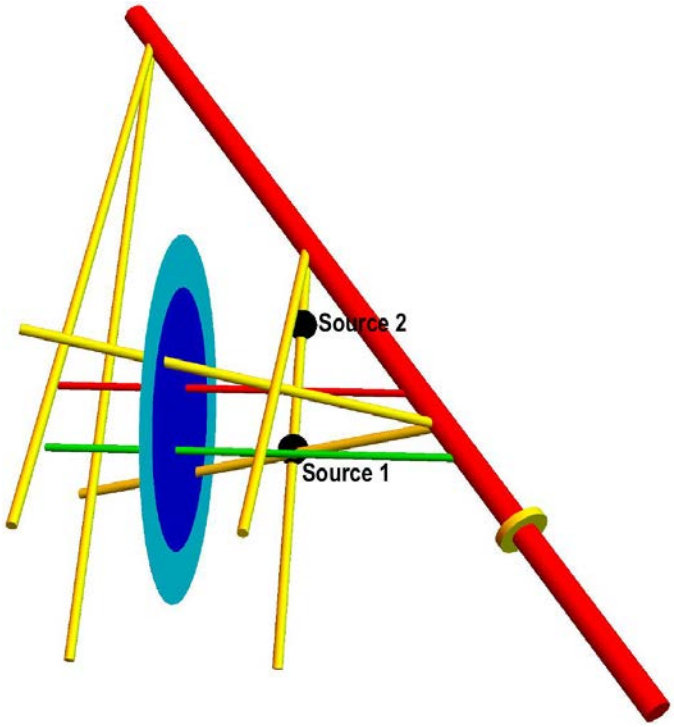

Figure 1: Schematic illustration of monitoring wells at SURF for the EGS Collab project. The monitoring wells drilled from the drift are in yellow. The well in green is the injection well, and the one in red is the production well. The circular region in blue is the fracture created by the injected water.

We use the following Thomsen parameters for the vertical transverse isotropic (VTI) medium in our numerical modeling:

V_{p0} = 4800 m/s,
V_{s0} = 3300 m/s,
ò = 0.417,
δ = 0.226,
γ = –0.206,

with density $\rho = 2850\,\text{kg/m}^3$. We build this VTI medium using laboratory measurements of core samples from the SURF site.

The slow qP-wave velocity direction (the symmetrical direction of the VTI medium, or normal of the background earth layer) is parallel with the strike or orientation of the fracture, i.e., fast qP-wave velocity direction is perpendicular to the fracture surface. The elasticity in GPa of the VTI medium is given by:

$$\mathbf{C} = \begin{bmatrix} 120.4125 & 58.3395 & -29.1698 & 0 & 0 & 0 \\ & 120.4125 & -29.1698 & 0 & 0 & 0 \\ & & 65.664 & 0 & 0 & 0 \\ & & & 52.6965 & 0 & 0 \\ & & & & 52.6965 & 0 \\ & & & & & 31.0365 \end{bmatrix}.$$

Figure 2 shows the group velocity curves on the $X-Y$ axis plane and on the $X-Z$ axis plane for the VTI medium used in our numerical modeling of elastic-wave sensitivity propagation.

We use our elastic-wave sensitivity modeling method (Denli and Huang, 2010; Gao and Huang, 2017) to compute the spatial distributions of elastic-wave sensitivity energies reflected/transmitted/scattered from the fracture plane. The elastic-wave sensitivity energy with respect to a given elastic parameter C_{ij} (i=1, … 6; j=1, …, 6) is computed using

$$\begin{aligned} E^{p}_{C_{ij}} &= \rho \tilde{V}_p^2 \, |\mathbf{U}^{p}_{C_{ij}}|^2, \\ E^{s}_{C_{ij}} &= \rho \tilde{V}_s^2 \, |\mathbf{U}^{s}_{C_{ij}}|^2, \end{aligned}$$

with $\tilde{V}$ represents the average phase velocities of qP- or qS-waves, and $\mathbf{U}_{C_{ij}}$ is the vector qP or qS sensitivity wavefield with respect to medium parameter C_{ij} separated using the low-rank vector decomposition for anisotropic medium, $|\mathbf{U}| = \sqrt{U_x^2 + U_y^2 + U_z^2}$.

We conduct numerical modeling of elastic-wave sensitivity propagation in a volume of 15 m $\times$ 15 m $\times$ 15 m with a spatial interval of 0.1 m along each axis of the Cartesian coordinates. Figure 3 displays two contour plots of the compressional- (left panel) and shear-wave (right panel) sensitivity energies with respect to elastic parameter C_{11} for a source located at Position 1 in Figure 1 for a fracture in blue with a diameter of 6 m. The value of elastic-wave sensitivity energy for the contour in red is the largest, and that in blue is the smallest. The values of the adjacent contours are different by a factor of 10. Figure 4 shows example cross-section plots of the compressional-wave (left panel) and shear-wave (right panel) sensitivity energies in Figure 3 for a source located at Position 1 in Figure 1.

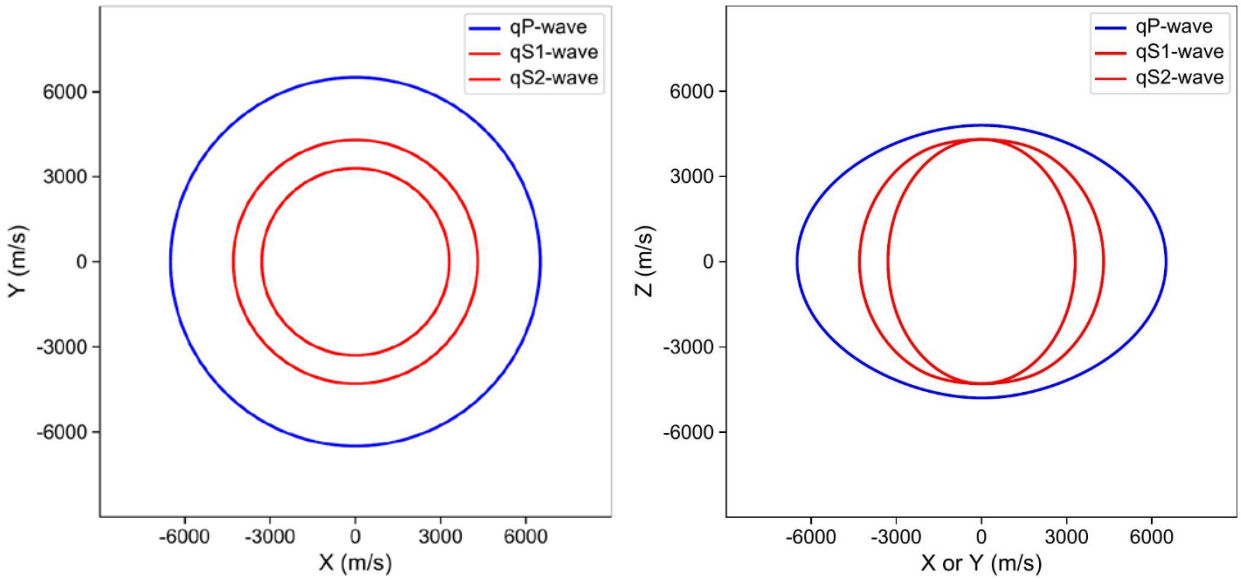

Figure 2: Group velocity curves on the X-Y axis plane (left panel) and the X-Z or Y-Z axis plane (right panel) for the VTI medium used for numerical modeling of elastic-wave sensitivity propagation at the SURF EGS experiment site. The plot on the X-Z axis plane is essentially the same with that on the Y-Z axis plane for the VTI medium.

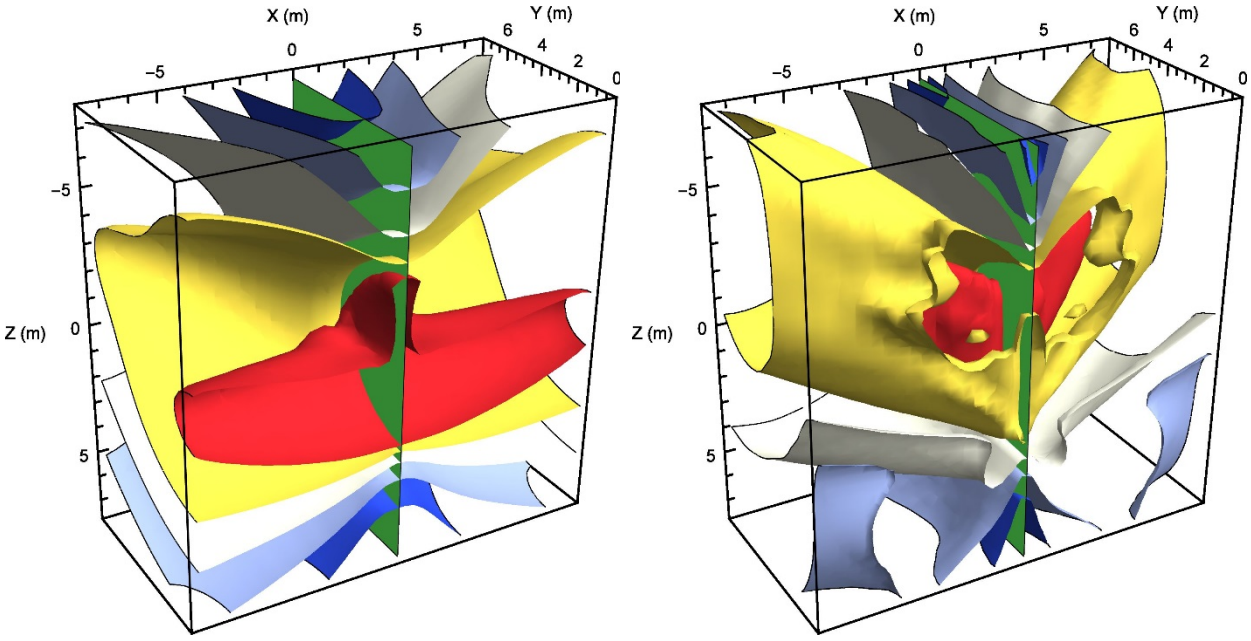

Figure 3: Contour plots of the compressional- (left panel) and shear-wave (right panel) sensitivity energies with respect to elastic parameter C_{11} for a source located at Position 1 in Figure 1. The value of elastic-wave sensitivity energy for the contour in red is the largest, and that in blue is the smallest. The increment value of the adjacent contours is 10 times of differences.

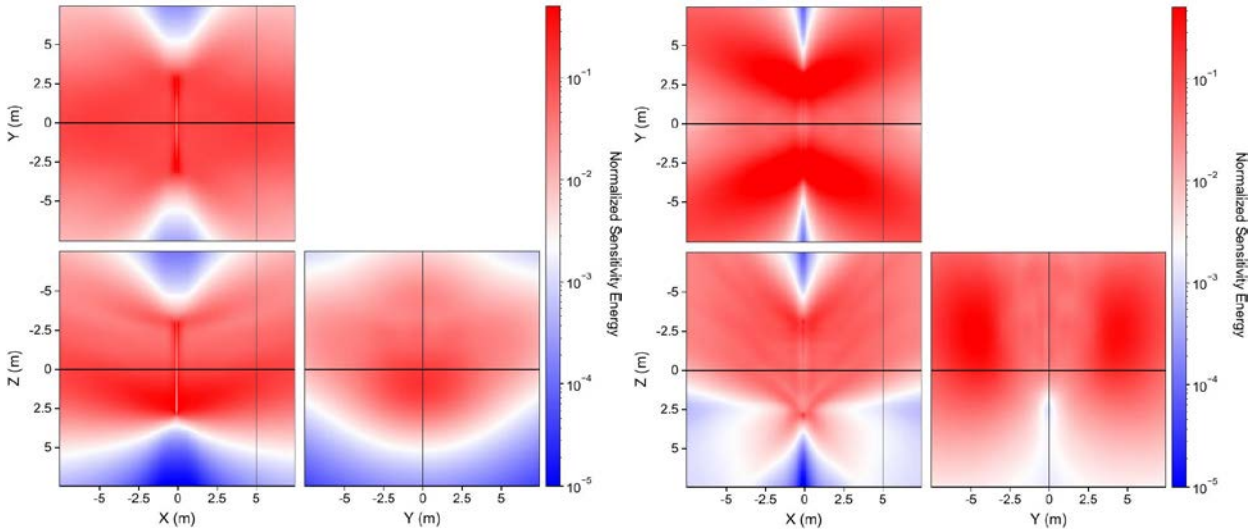

Figure 4: Example cross-section plots of the compressional-wave (left panel) and shear-wave (right panel) sensitivity energies in Figure 3 for a source located at Position 1 in Figure 1.

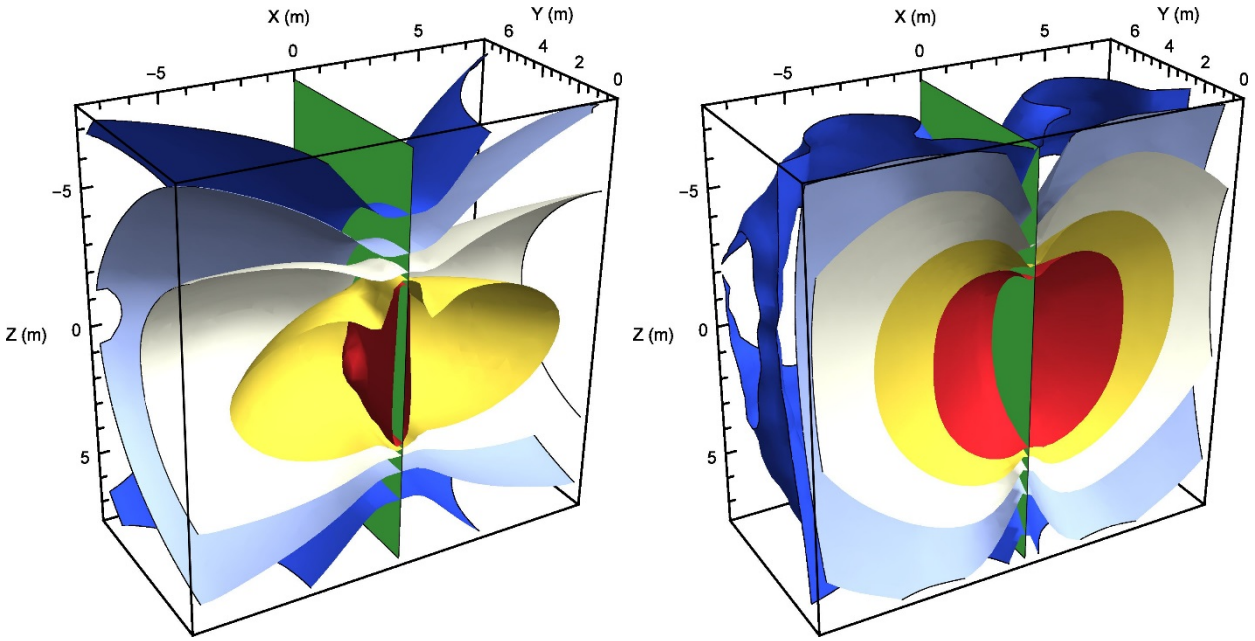

Figure 5: Contour plots of the compressional- (left panel) and shear-wave (right panel) sensitivity energies with respect to elastic parameter C_{11} for a source located at Position 2 in Figure 1. The value of elastic-wave sensitivity energy for the contour in red is the largest, and that in blue is the smallest. The increment value of the adjacent contours is 10 times of differences.

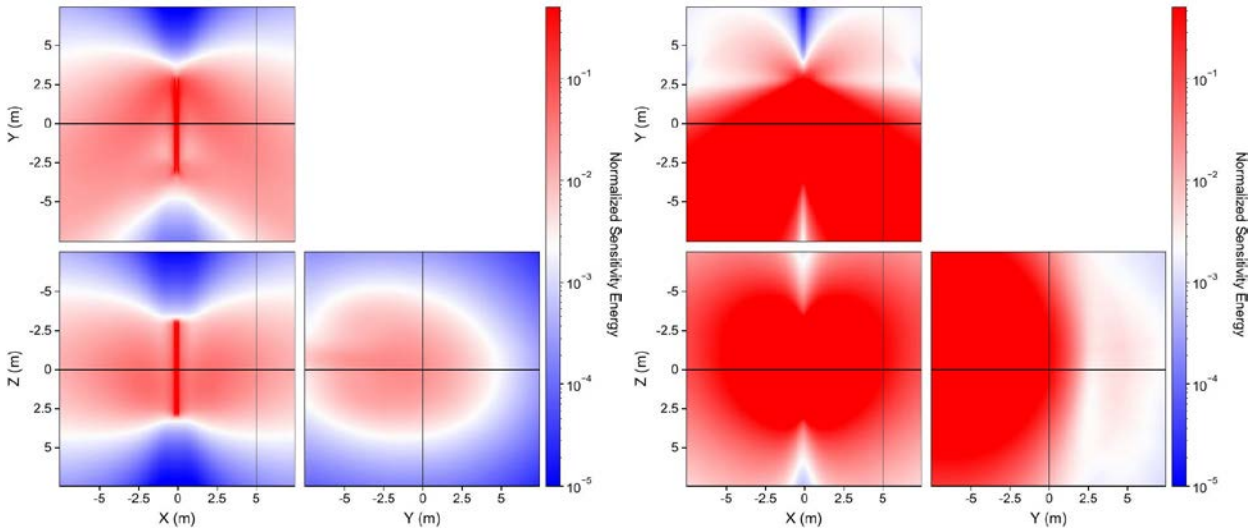

Figure 6: Example cross-section plots of the compressional-wave (left panel) and shear-wave (right panel) sensitivity energies in Figure 5 for a source located at Position 2 in Figure 1.

Figure 5 depicts two contour plots of the compressional- (left panel) and shear-wave (right panel) sensitivity energies with respect to elastic parameter C_{11} for a source located at Position 2 in Figure 1 for a fracture in blue with a diameter of 6 m. Comparing Figure 3 and Figure 5, we observe that the spatial distributions of elastic-wave sensitivity energies for different source locations are significant different.

Figure 6 displays example cross-section plots of the compressional-wave (left panel) and shear-wave (right panel) sensitivity energies in Figure 5 for a source located at Position 2 in Figure 1.

To record significant acoustic-/elastic-wave signals scattered from the fracture, geophones should be placed within the region inside the red contour in the contour plots, or within the red regions in the cross-section plots of elastic-wave sensitivity energy distributions, as depicted in Figure 3 to Figure 6.

3. Optimal Design of Passive Seismic Monitoring Network

For optimal design of passive seismic monitoring network, we study the relationships between spatial location errors and induced micro-earthquakes (MEQ) during the stimulation process at the SURF experiment site.

We develop an analytical method to calculate the travel-time arrivals in the homogeneous and anisotropic medium. For the VTI medium, we set the P-wave velocities along the fast and slow axes to be 6.5 km/s and 4.8 km/s, and the S-wave velocities along the fast and slow axes to be 4.3 km and 3.3 km. We calculate the stiffness matrix C_{ij} in the transversely isotropic case. We then adopt the Kelvin-Christoffel equation to estimate the slowness of the P- and S- wave in the specific direction (Carcione, 2007). The slowness can be used to obtain the P and S arrival times for any locations in this homogenous, anisotropic medium.

We perform a non-linear inversion to obtain micro-earthquake locations using travel times. The inversion method adopts a simulated heat annealing algorithm (Chen et al, 2014) to search for the best hypocentral location for a given event. The method minimizes the least-square misfits between the predicted and observed P- and S-wave arrival times.

We study the relationships between the MEQ spatial location errors (standard deviation errors) and the geophone distribution configurations for various scenarios as shown in Figure 7. We use a total of 319 MEQs evenly distributed within the fracture shown in blue in Figure 7. The distance between MEQs along each axis of the Cartesian coordinate is 0.5 m. The diameter of the circular fracture in blue in each panel of Figure 7 is 10 m. The distance between and the fracture plane and the motoring wells parallel with the fracture is 5 m. We assume that the geophone are distributed within 15 m in the monitoring wells centered approximately on the area of the fracture.

We first study the optimal open angle between the two monitoring wells. We use two monitoring wells with a distance of 10 m from the intersection with the drift to the center of the created fracture for this study, as shown in the top-left panel in Figure 7. Figure 8 shows the standard deviation errors of micro-earthquakes vs the open angles for the monitoring wells parallel with (left panel) and perpendicular to (right panel) the created fracture. The solid line in each panel of Figure 8 is for the noise-free case, and the dashed line is for the case of noisy travel-time picks, which have a Gaussian distribution with a standard deviation of $5x10^{-5}$ seconds. The results in Figure 8 show that the open angle of $30°$ is a good choice for passive monitoring.

We use the open angle of $30°$ for the monitoring wells for our study of the relationship between the standard deviation errors of MEQ event locations and the geophone distributions. Figure 9 shows the relationships between the standard deviation error of micro-earthquake event locations and the total numbers of geophones evenly distributed within the monitoring wells in each scenario as shown in Figure 7. In each panel in Figure 9, the solid line is for noise-free travel-time picks, and the dashed line is for noisy travel-time picks, which have a Gaussian distribution with a standard deviation of $5x10^{-5}$ seconds. We plot all curves in Figure 9 together in Figure 10. The results demonstrate that we should use 8 geophones evenly distributed within four wells parallel with (blue curve) or perpendicular to (green curve) the fracture plane (two geophones in each well). The combination of parallel and perpendicular wells does not help with MEQ event location. Note that the errors in velocity values do not change the aforementioned conclusions even though the errors may change the standard deviation errors of MEQ event locations.

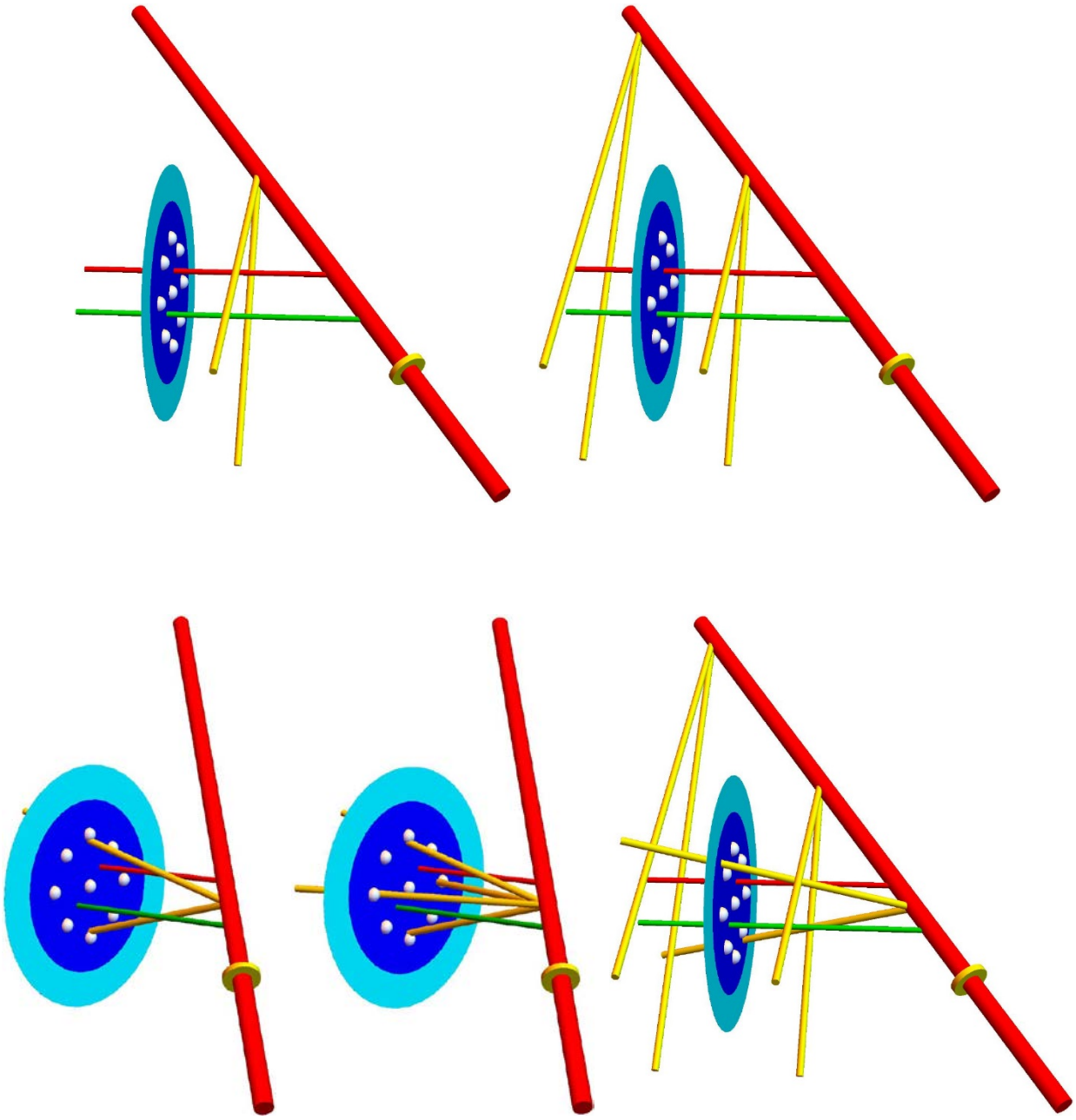

Figure 7: Various borehole scenarios for passive seismic monitoring at the SURF experiment site. The geophones are distributed within the monitoring wells in yellow to monitor induced micro-earthquakes depicted by white balls within the created fracture in the blue circular region.

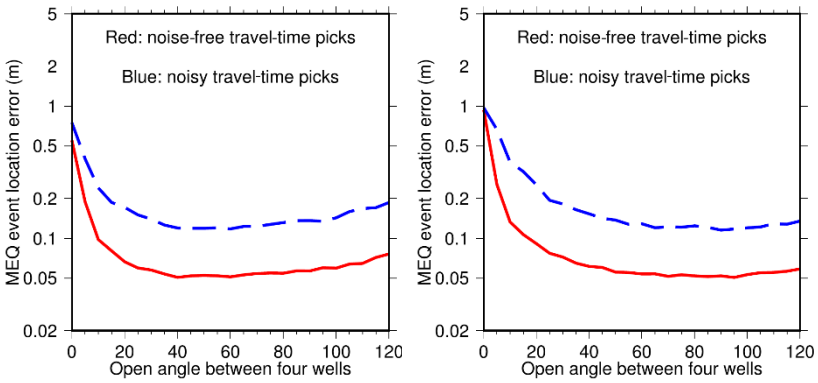

Figure 8: Standard deviation error of micro-earthquakes vs the open angle for the monitoring wells parallel with (left panel) and perpendicular to (right panel) the created fracture. In both cases, the open angle of $30°$ is a good choice for passive monitoring.

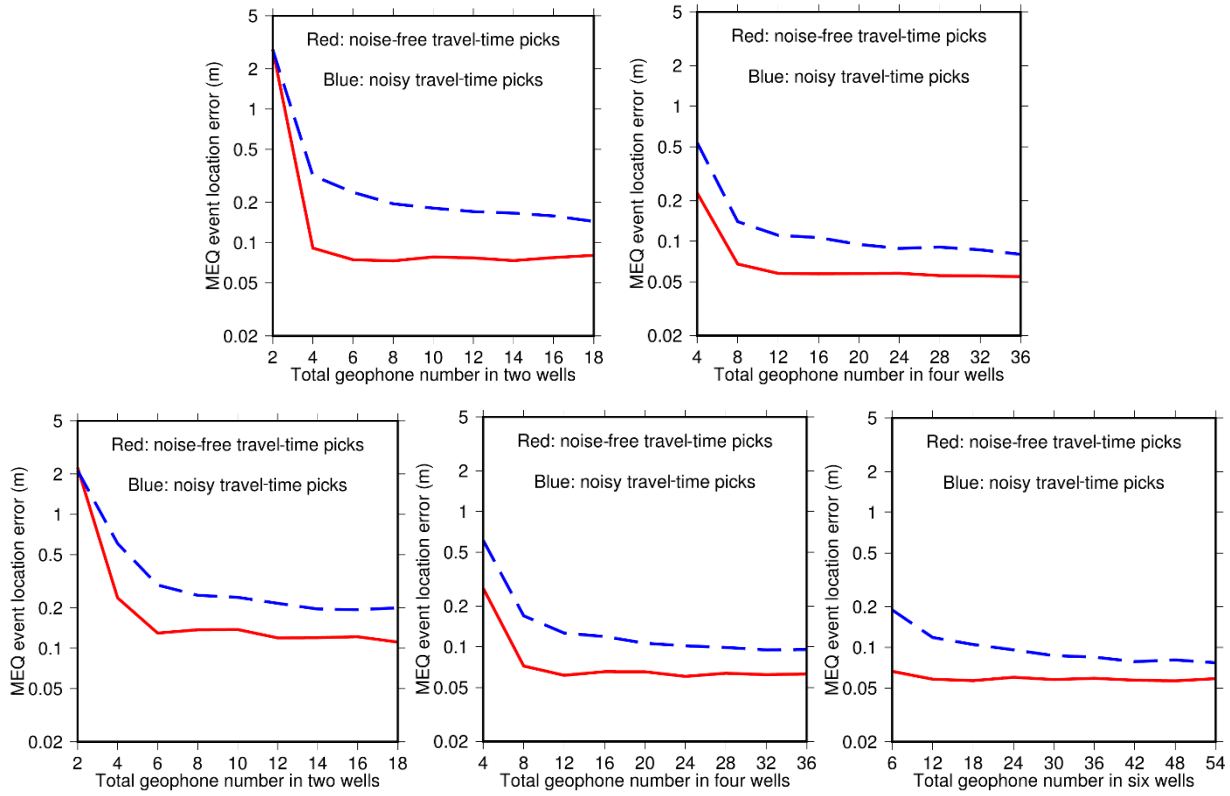

Figure 9: Standard deviation errors of micro-earthquake event locations vs the total numbers of geophones evenly distributed within the monitoring wells as shown in Figure 7. Each panel corresponds to each of those in in Figure 7. The solid line in each panel is for noise-free travel-time picks, and the dashed blue line is for noisy travel-time picks.

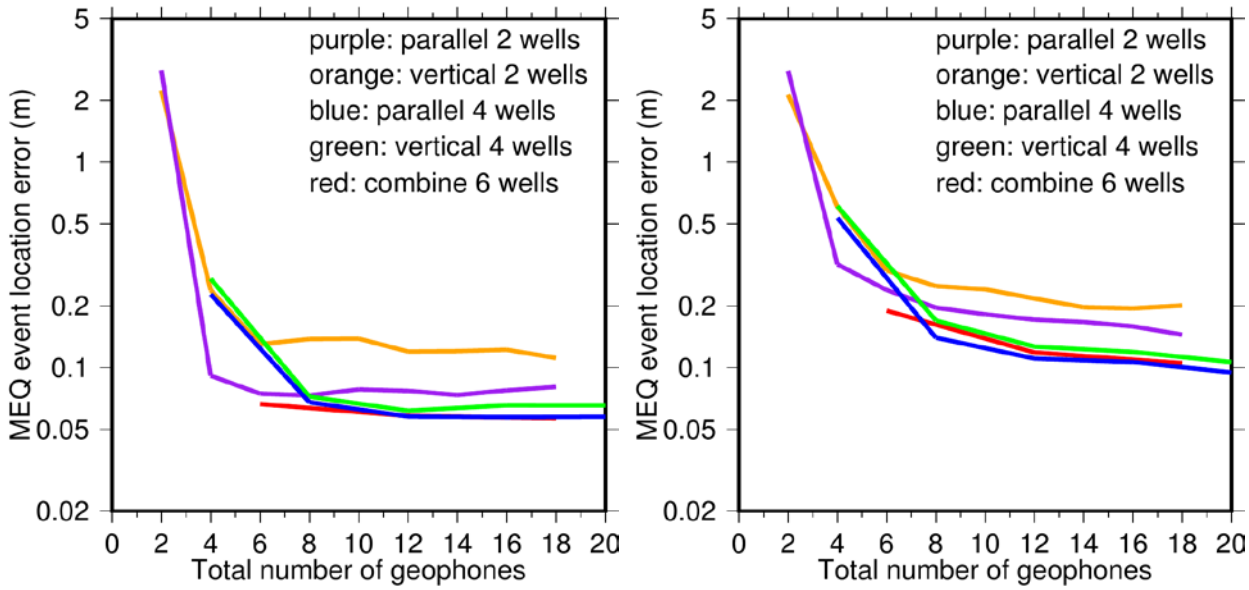

Figure 10: Standard deviation errors of micro-earthquake event locations vs the total numbers of geophones evenly distributed within the monitoring wells as shown in Figure 7 for noise-free travel-time picks (left panel) and noisy travel-time picks (right panel).

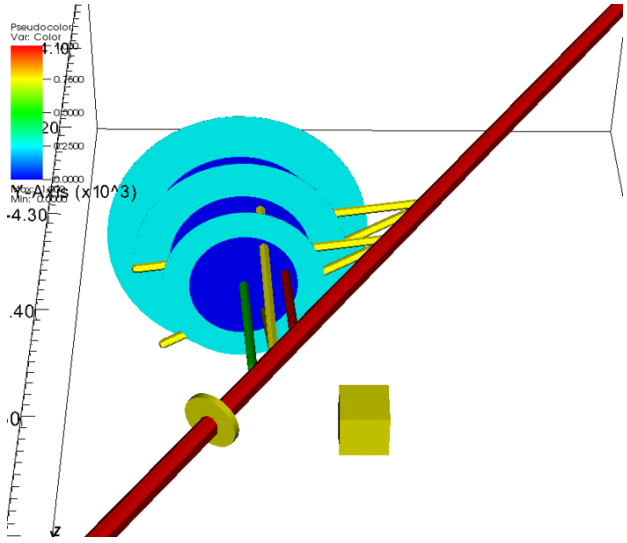

Figure 11: Schematic illustration of the EGS Collab experiments. The water injection well is in green, the production well is in red, the circular planes represent the expected extents of the hydraulic fractures (deep blue, 15 m in radius) and those with a 5 m error margin in radius estimation (light blue), and the wells in yellow are monitoring wells. The existing drift of is in red and small yellow disk marks the location of a planned blast door. The yellow cube (10 m x 10 m x 10 m) annotates the length scale.

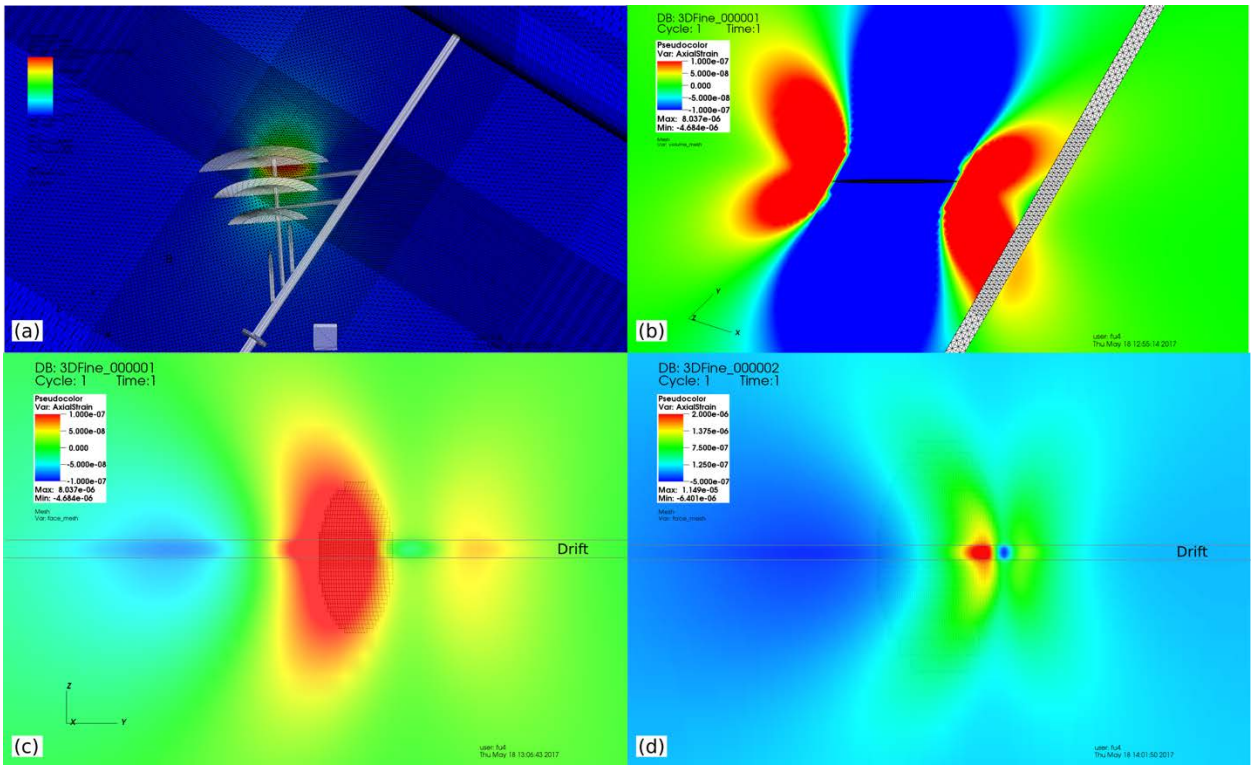

Figure 12: FEM simulation results of axial strain on the drift wall. (a) The displacement (perpendicular to fracture plane) field overlaid on the FEM mesh and the preliminary design shown in Figure 11. Note that the FEM model used round numbers for angles and therefore does not align perfectly with the design. (b) The tensile strain (parallel to the drift) displacement distribution assuming a 15 m radius fracture and 200 kPa net pressure, on a horizontal plane cutting the mid-height of the drift. The color scale saturates at ±0.1 micro-strain. (c) The same displacement field as (b) on a vertical plane cutting along the west-side wall of the drift. (d) The tensile strain (parallel to the drift) displacement distribution assuming a 30 m radius fracture and 200 kPa net pressure, on a vertical plane cutting along the west-side wall of the drift. The color scale saturates at 2.0 positive micro-strain (tensile) and -0.5 micro-strain (compressive). In (c) and (d), the hydraulic fracture is shown as a meshed circular surface.

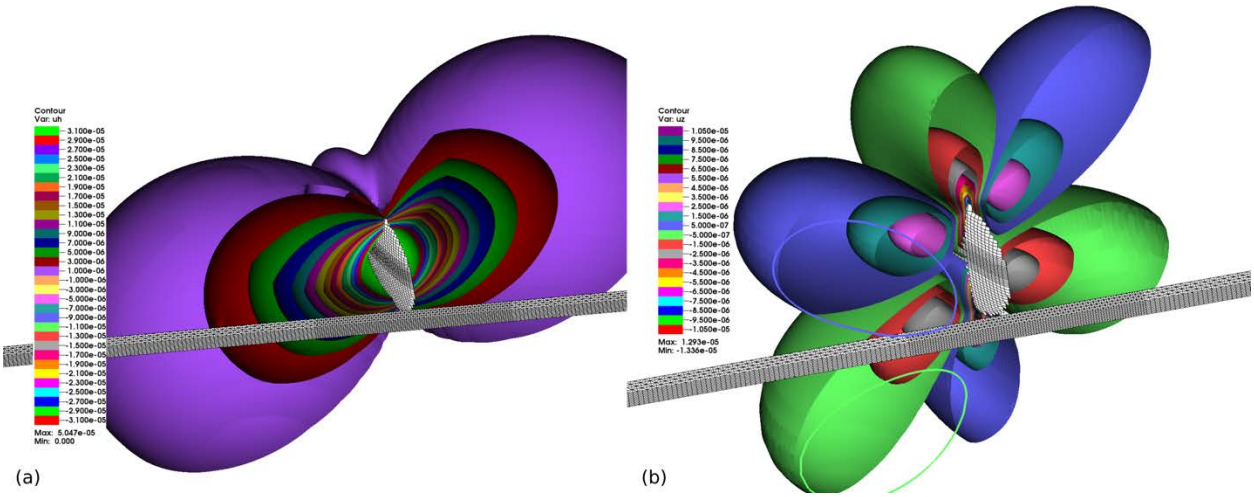

Figure 13: Contours of (a) horizontal displacement field and (b) vertical displacement (in meter) field around the hydraulic fracture (15 m in radius, subjected to 200 kPa net pressure). In (a), the increment between contour surfaces is 2.0 microns and in (b), the interval is 0.5 microns.

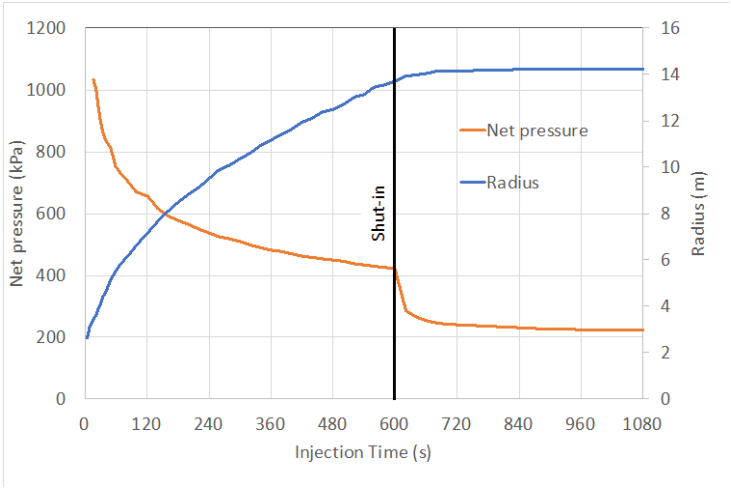

Figure 14: FEM simulation result of axial strain in wells perpendicular to the fracture plane.

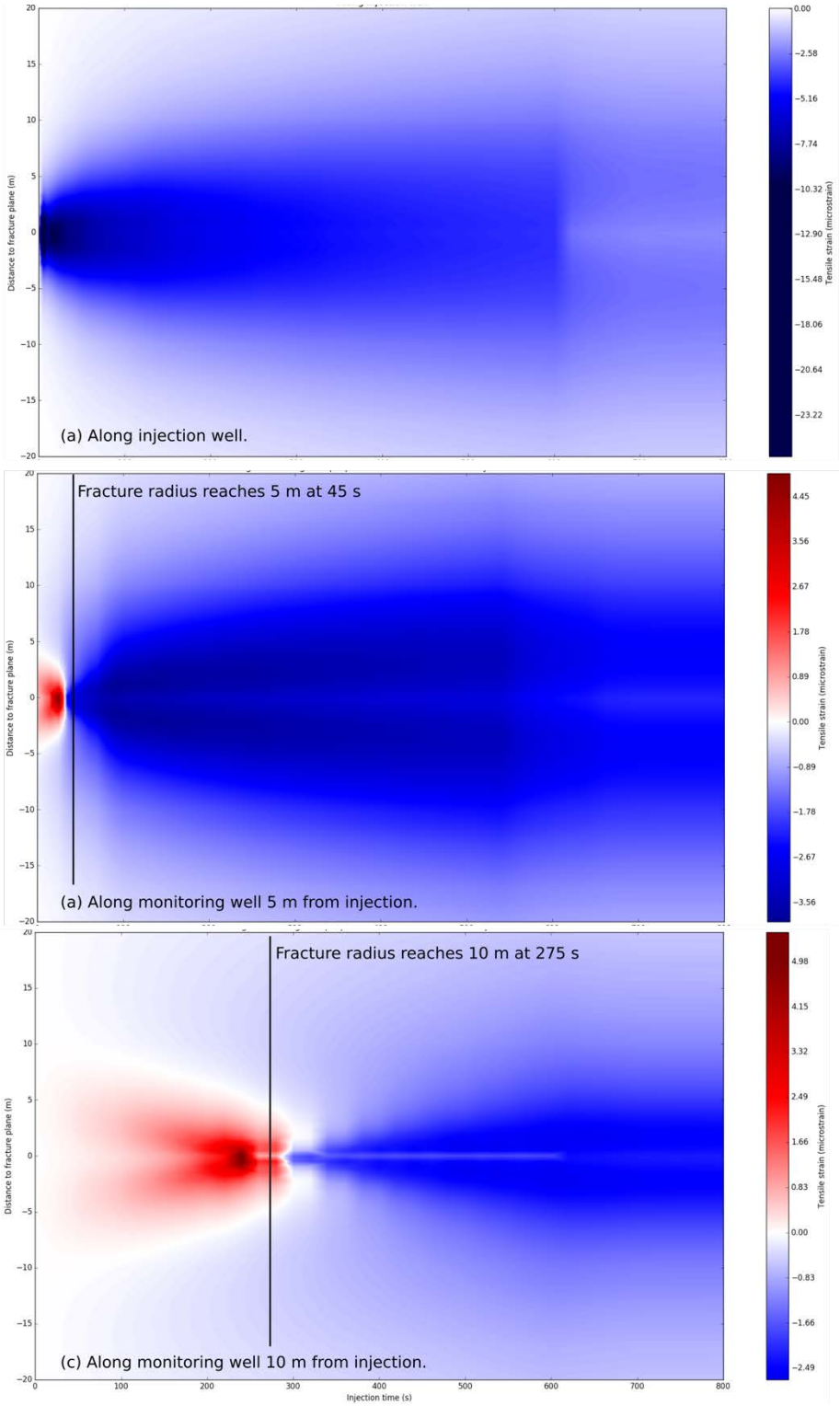

Figure 15: FEM simulation result of the axial strain in the (a) injection well, (b) a monitoring well 5 m from the injection well, and (c) a monitoring well 10 m from the injection well. Note that only the continuum strain along the wellbore is depicted while significant displacement discontinuity takes place where the fracture intersects the wellbores. Each sub-figure has a different color scale. Red is in tension and blue in compression.

4. Feasibility of Using Alternative Displacement-Type Measurement to Monitor Hydraulic Fracture Growth

We conduct numerical modeling of various displacement responses of the rock body subjected to the expected hydraulic stimulation operation. Responses investigated as potential monitoring means of hydraulic fracture growth include tensile strains along the drift wall, "tilts" measured by tiltmeter arrays, and axial strains in injection, production, and monitoring wells. The modeling results can be used to inform the design and optimization of experiment instrumentation at SURF (Figure 11). All simulations are performed using LLNL's GEOS code (Settgast et al., 2017)

For the tiltmeter and drift wall strain analyses, we mesh a rock block 450 m x 450 m x 200 m around the drift with 0.3 m resolution (near-field) finite elements (10M elements in total), and model the deformation field of a statically pressurized fracture (with a net pressure of 200 kPa) using the finite-element method (FEM). We assume an isotropic, linearly elastic rock medium with a Young's modulus of 71.4 GPa and Poisson's ratio of 0.22. Figure 12 shows FEM simulation results of axial strain on the drift wall for two scenarios, fracture radius being 15 m (expected design) and fracture radius being 30 m (fracture front approaching the drift wall). We find that in the former scenario, the tensile strain on the drift wall is at the 0.1 microstrain level. If the fracture growth approaches the drift wall, it's possible to measure 1 microstrain on the wall. However, because of the expected disassociation of the drift wall rock to the intact rock body caused by local damages, the actual measured strain is likely to be much smaller and noisy.

A tiltmeter measures the horizontal gradient of a vertical displacement field (du_v/dh) or the vertical gradient of a horizontal displacement field (du_h/dv). In oil and gas field applications, an array of tiltmeters is often placed in a vertical well next to the well being stimulated to monitor the hydraulic fracture's height growth (Wright et al., 1998; Hejl et al. 2007). Ground surface tiltmeter arrays are also often used to infer the strike directions of hydraulic fractures (Hejl et al. 2007). Figure 13 shows contours for horizontal and vertical displacements around the fracture. In Figure 13(a), along any imaginary vertical wellbore, the measured tilt is the contour interval (2 microns) divided by the distance between the adjacent contour surfaces intersected by the well. The most useful measurement would be along a wellbore right next to the fracture, which is impractical for the EGS Collab experiement plan. Along the existing kISMET wellbores, some tilts could be detected but the results do not correspond to the extent the fracture in any direct way. Based on the vertical displacement field in Figure 13(b), a 2D array in the horizontal wells above the fracture can capture the strike of the fracture but cannot be used to estimate fracture size, and is therefore of minimal value to this research project.

For wellbore axial strain measurements, we simulate the propagation of a hydraulic fracture under an injection rate of 0.1 liter/s, which reaches a radius of 15 m after 10 minutes of stimulation. We simulate the fracture's shut-in response after 10 minutes of injection. The fracture's responses in terms of fracture radius and net fluid pressure are shown in Figure 14. Figure 15 depicts the FEM simulation result of the axial strain in the wells perpendicular to the fracture plane. In the injection well, compressive strain greater than 10 microstrains develops at the early stage of the stimulation when the net pressure is higher. In each monitoring well, tensile strain up to 5 microstrains develops as the fracture tip approaches the well, and up to 5 microstrains of compressive strain develops near the fracture plan as the fracture passes the well.

Note that results in Figure 15 do not include the dilation of the fracture, which is considered a discontinuity in the displacement instead of strain in the continuum.

5. Conclusions

We have conducted preliminary numerical modeling of active and passive seismic monitoring, and studied the feasibility of using alternative displacement-type measurement for monitoring hydraulic fracturing growth at the EGS Collab experiment site. Our elastic-wave sensitivity modeling in anisotropic media can provide the best locations to record significant reflected/transmitted/scattered wavefields from the fracture plane during active seismic surveys. Our passive seismic monitoring analyses for micro-earthquake locations demonstrate that, for cost-effective monitoring, we should use 8 geophones evenly distributed within four monitoring wells parallel with or perpendicular to the fracture plane (two geophones in each well). The combination of parallel and perpendicular wells does not help with MEQ event location. Our finite-element simulations demonstrate that it will be challenging to detect the small tensile strain along the drift wall caused by the hydraulic stimulation, although a hydraulic fracture approaching the drift could induce relatively large, localized strain signals. The monitoring wells in current design are not ideal for tiltmeter monitoring. The axial strain along perpendicular monitoring wells is generally below 5 microstrains, but the change of the signs of the axial strain could be used to signal the approaching and passing of the hydraulic fracture.

ACKNOWLEDGMENTS

This project is supported by the U.S. Department of Energy, Office of Energy Efficiency and Renewable Energy (EERE), Geothermal Technologies Office (GTO) through contract No. DE-AC52-06NA25396 to Los Alamos National Laboratory (LANL), contract No. DEAC02-05CH11231 to Lawrence Berkeley National Laboratory, and contract No. DE-AC52-07NA27344 to Lawrence Livermore National Laboratory. The computation was performed using super-computers of LANL's Institutional Computing Program as well as facilities of LLNL's Livermore Computing Center.

REFERENCES

Kneafsey, T., et al., " An Introduction to the EGS Collab SIGMA-V Project: Stimulation Investigations for Geothermal Modeling Analysis and Validation," *GRC Transactions*, 41, (2017).

Daley, T. M., Solbau, R. D., Ajo-Franklin, J. B., and Benson, S. M. "Continuous active-source seismic monitoring of CO_2 injection in a brine aquifer." *Geophysics, 72(5):A57–A61*, (2007)

Denli, H., and Huang, L., "Elastic-wave sensitivity propagation." *Geophysics*, 75, (2010), T83-T97.

Gao, K. and Huang, L., "Monitoring fracture zones using anisotropic elastic-wave sensitivity." *Geophysical Journal International*, under review, (2017).

Carcione, José M. "*Wave fields in real media: Wave propagation in anisotropic, anelastic, porous and electromagnetic media*." Vol. 38. Elsevier, (2007).

Chen, Y., Wen, L., and Chen, J. "A cascading failure during the 24 May 2013 great Okhotsk deep earthquake." *Journal of Geophysical Research: Solid Earth*, 119.4, (2014), 3035-3049.

Wright, C. A., Davis, E. J., Weijers, L., Golich, G. M., Ward, J. F., Demetrius, S. L., and Minner, W. A. (1998). "Downhole Tiltmeter Fracture Mapping: A New Tool for Directly Measuring Hydraulic Fracture Dimensions". In *SPE Annual Technical Conference and Exhibition*, 27-30 September, New Orleans, Louisiana. SPE-49193-MS.

Hejl, K., Madding, A., Morea, M., Glatz, C., Luna, J., Minner, W., … Stanley, G. (2007). "Extreme multistage fracturing improves vertical coverage and well performance in the Lost Hills field." *SPE Drilling & Completion*, 22(4), SPE-101840-PA.

Settgast, R.R., Fu, P., Walsh, S.D.C., White, J.A., Annavarapu, C., and Ryerson, F.J. (2017). "A fully coupled method for massively parallel simulation of hydraulically driven fractures in 3-dimensions." *International Journal for Numerical and Analytical Methods in Geomechanics*, 41(5), 627–653.